

Partially-Bright Triplet Excitons in Perovskite Nanocrystals

A. Liu,^{1,*} D. B. Almeida,^{1,*} L. G. Bonato,² G. Nagamine,³ L. F. Zagonel,³ A. F. Nogueira,² L. A. Padilha,^{3,†} and S. T. Cundiff^{1,‡}

¹*Department of Physics, University of Michigan, Ann Arbor, Michigan 48109, USA*

²*Instituto de Química, Universidade Estadual de Campinas, 13083-970 Campinas, Sao Paulo, Brazil*

³*Instituto de Física “Gleb Wataghin”, Universidade Estadual de Campinas, 13083-970 Campinas, Sao Paulo, Brazil*

(Dated: May 24, 2022)

Advances in opto-electronics require the development of materials with novel and engineered characteristics. A class of materials that has garnered tremendous interest is metal-halide perovskites, stimulated by meteoric increases in photovoltaic efficiencies of perovskite solar cells. In addition, recent advances have applied perovskite nanocrystals (NCs) in light-emitting devices. It was discovered recently that, for cesium lead-halide perovskite NCs, their unusually efficient light-emission may be due to a unique excitonic fine-structure composed of three bright triplet states that minimally interact with a proximal dark singlet state. To study this fine-structure without isolating single NCs, we use multi-dimensional coherent spectroscopy at cryogenic temperatures to reveal coherences involving triplet states of a CsPbI₃ NC ensemble. Picosecond timescale dephasing times are measured for both triplet and inter-triplet coherences, from which we infer a unique exciton fine-structure level-ordering comprised of a dark state energetically positioned within the bright triplet manifold.

INTRODUCTION

Cesium lead-halide perovskites were first synthesized over a century ago with a general chemical formula CsPbX₃ (where X = Cl, Br, or I). Recently, synthesis of CsPbX₃ nanocrystals (NCs) was achieved [1, 2], which combines the advantages of perovskites (e.g., efficient luminescence, long carrier diffusion length) with that of colloidal NC materials (e.g., surface engineering, size-tunable emission). Perovskite NCs exhibit luminescence with quantum yields reaching nearly unity [3], in contrast to the optimized 80% quantum yield achieved by chalcogenide NCs coated with a gradient shell [4]. Although all other colloidal materials suffer inhibited emission from lower energy dark states [5], the unusual brightness of perovskite NCs is now believed to originate from an optically active, nondegenerate triplet state that emits efficiently despite the presence of a dark singlet state [6, 7].

The unique exciton fine-structure of perovskite NCs has significantly extended the potential applications of colloidal NCs. In particular, the three non-degenerate bright triplet states and their orthogonally-oriented dipole moments have generated much excitement for potential applications in quantum information processing [8, 9]. However, engineering exciton superposition states as information carriers will require an intimate knowledge of their coherent dynamics, which are still not well-understood. The exciton fine structure of perovskite NCs has thus far only been studied via single-NC photoluminescence [6, 10, 11] and transient absorption [12, 13] techniques, which have provided information only about their incoherent population dynamics. Furthermore, inhomogeneous spectral broadening due to NC size dispersion limits the utility of linear spectroscopic techniques in studying NC ensembles. More sophisticated methods

are thus required [14–17] to extract the desired ensemble-averaged coherent properties of perovskite NCs.

Here, we extract crucial figures of merit for quantum information processing, the ensemble-averaged triplet coherence times, and reveal coherence times of both optical triplet coherences and terahertz inter-triplet coherences for an ensemble of CsPbI₃ NCs (see Fig. 1a-b) at cryogenic temperatures. We also present evidence for a mixed bright-dark level-ordering (see Fig. 1c) that renders the triplet state excitons only partially bright. These measurements are enabled by using multi-dimensional coherent spectroscopy (MDCS) [18] to circumvent the inhomogeneous broadening that obscures spectral signatures of the exciton fine-structure and resolve coherent coupling involving different triplet states. The extracted coherence times for CsPbI₃ NCs are an order-of-magnitude longer compared to candidate materials for valley-tronics [14, 15, 19], which positions perovskite NCs as a potential material platform for quantum information applications via bottom-up assembly.

To perform MDCS we use a Multi-Dimensional Optical Nonlinear Spectrometer [21], which focuses three laser pulses onto the perovskite NC ensemble sample as a function of three time delays τ , T , and t (schematically shown in Fig. 1d and inset). By Fourier transforming the emitted four-wave mixing (FWM) signal as a function of two or all three time delays, the coherences and populations induced by each pulse are correlated in a multi-dimensional spectrum. In this study, we Fourier transform along the variables τ and t to obtain one-quantum spectra (which correlate the absorption energy $\hbar\omega_\tau$ with the emission energy $\hbar\omega_t$) and along the variables T and t to obtain zero-quantum spectra (which correlate the intraband mixing energy [22] $\hbar\omega_T$ and the emission energy $\hbar\omega_t$). Furthermore, the polarization of the second pulse

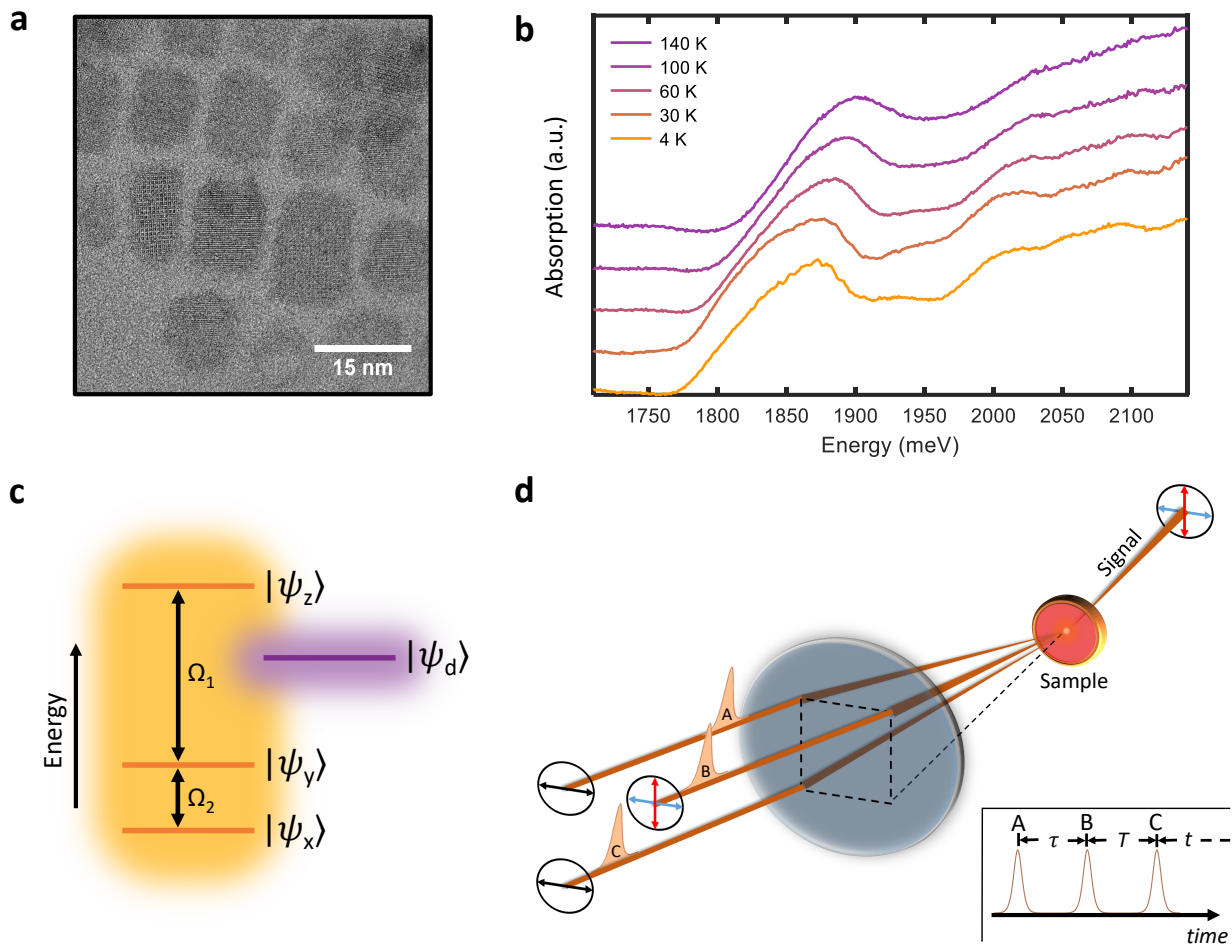


FIG. 1: **CsPbI₃ perovskite nanocrystals studied via MDCS.** **a**, Transmission electron micrograph of representative CsPbI₃ NCs. **b**, Perovskite NC absorption spectra as a function of temperature [20]. **c**, Energy level diagram of the non-degenerate bright triplet states $\{\psi_x, \psi_y, \psi_z\}$ that form the band-edge. The dark singlet state $|\psi_d\rangle$ is shown to lie between states $|\psi_y\rangle$ and $|\psi_z\rangle$, which is argued in the main text. **d**, Schematic of the MDCS experiment. Three pulses A, B, and C arranged in the box geometry are focused onto the sample with varying time delays as shown in the inset. Double-sided arrows in circles denote the polarization of each pulse. Pulses A and C are horizontally polarized, which is indicated by the horizontal arrows. Pulse B is either horizontally or vertically polarized, which corresponds to an emitted signal of either horizontal or vertical polarization respectively as indicated by arrows of matching color of the emitted signal.

(labeled B in Fig. 1d) is chosen to align either parallel or orthogonal to the co-linear polarizations of the other two pulses to probe different quantum pathways. We denote the two polarization schemes as co-linear excitation and cross-linear excitation respectively.

ONE-QUANTUM SPECTRA PROBE OPTICAL TRIPLET COHERENCES

One-quantum spectra were acquired at a temperature of 4.6 K with co-linear and cross-linear excitation (shown in Figs. 2a and 2b). Both spectra show numerous peaks that are elongated in the diagonal direction ($|\hbar\omega_\tau| = |\hbar\omega_t|$), reflecting inhomogeneous broadening [23]. By taking cross-diagonal slices (indicated by

the red/white dashed lines in Figs. 2a and 2b), the ensemble-averaged homogeneous response of NCs with a certain resonance energy is obtained [23]. We plot cross-diagonal slices of the one-quantum spectra in Figs. 2c and 2d. In the full slices (inset), asymmetric peaks are observed for $|\Delta E| \gtrsim 4$ meV which we attribute to electronic-vibrational coupling. The main plots of each slice section (highlighted by the yellow boxes inset) show symmetric peaks that, due to their polarization dependence, we attribute to absorption and emission involving different triplet state coherences.

In the third-order perturbative limit, the origin of observed peaks is interpreted as changes in the system density matrix induced by each pulse that form accessible quantum pathways [24]. Peaks 1 and 3 in Fig. 2c are generated by absorption and emission of coherences in-

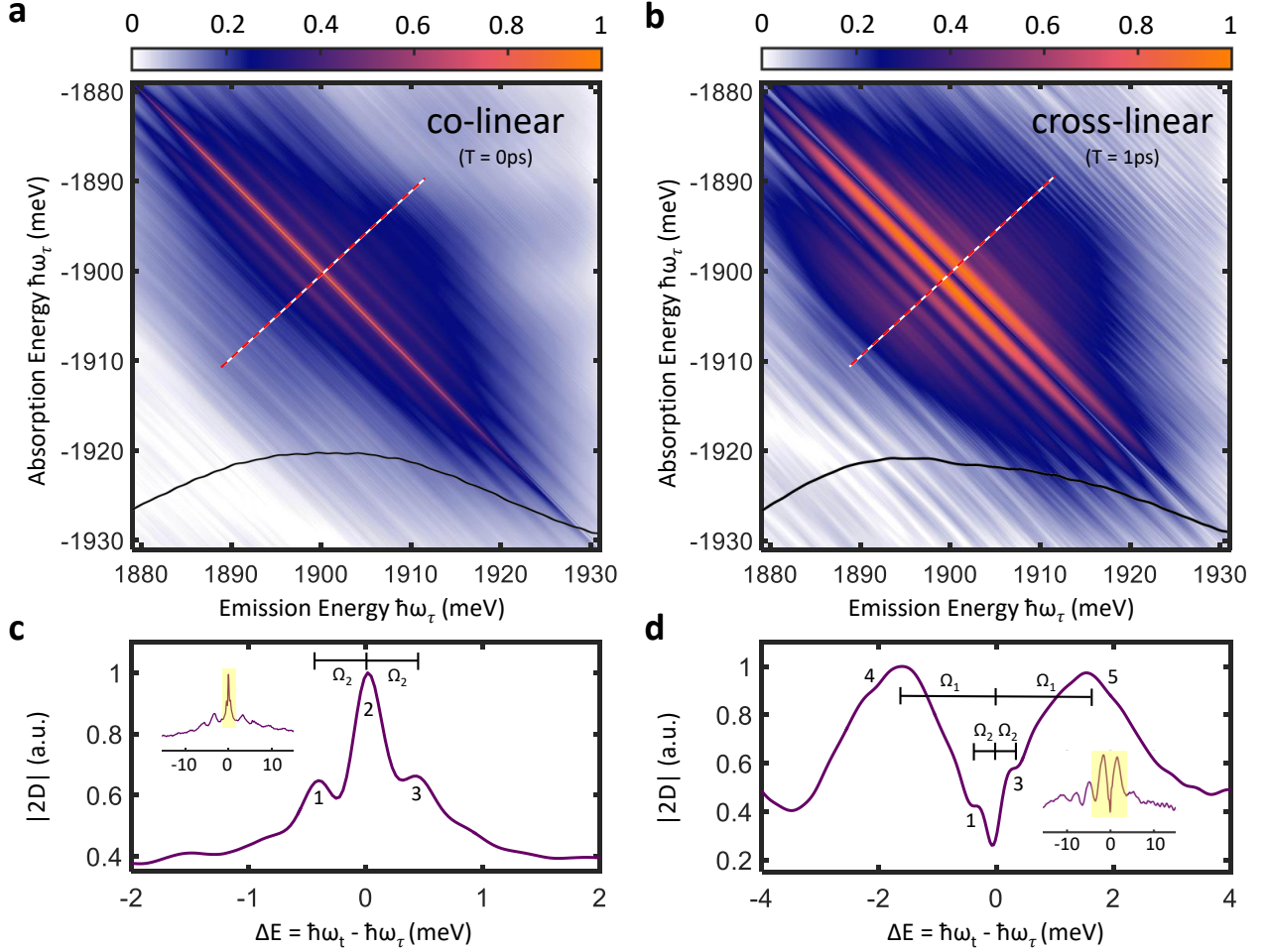


FIG. 2: **Triplet coherences in one-quantum spectra.** Magnitude one-quantum spectrum at 4.6 K with **a**, co-linear and **b**, cross-linear excitation. The white/red dashed lines and solid black lines indicate the cross-slice locations and laser pulse spectra respectively. Cross-slice centered at $|\hbar\omega_i| = |\hbar\omega_\tau| = 1900$ meV of the **c**, co-linear and **d**, cross-linear excitation one-quantum spectrum. Numbers in **c** and **d** indicate peaks arising from electronic interband coherences and populations.

volving $|g\rangle$ and both triplet states $|\psi_x\rangle$ and $|\psi_y\rangle$. We note that our measurements do not inform the ordering of states $|\psi_{x/y}\rangle$, so we assume the ordering shown in Fig. 1c for labeling the dephasing rates discussed below. The central peak 2 is likewise generated by quantum pathways involving absorption and emission by coherences of identical resonance energy $|g\rangle\langle\psi_i|$ and $|\psi_i\rangle\langle g|$ respectively. In Fig. 2d peaks 1 and 3 are visible as shoulders on two new peaks 4 and 5, which are generated by absorption and emission of coherences involving $|g\rangle$ and triplet states $|\psi_y\rangle$ and $|\psi_z\rangle$. The polarization dependence of all five peaks reflects orthogonally-oriented linear dipole moments of the three triplet states. Here, the peak strengths are determined by the projection of each dipole moment onto the observation plane of each NC. However, the absence of a clear sideband at $\Delta E = \pm(\Omega_1 + \Omega_2)$, corresponding to coupling between the transitions involving $|g\rangle$ and triplet states $|\psi_x\rangle$ and $|\psi_z\rangle$, suggests a much stronger dipole moment for $|\psi_y\rangle$ compared to those of

$|\psi_x\rangle$ and $|\psi_z\rangle$.

Fitting the cross-diagonal lineshapes also extracts the homogeneous linewidths γ_i [23] of triplet state transitions between $|g\rangle$ and $|\psi_i\rangle$. In this context one-quantum spectra are particularly useful when compared to integrated FWM techniques [25], since the cross-diagonal slice position $|\hbar\omega_i| = |\hbar\omega_\tau|$ reflects an effective NC size (see SI). Though the peaks 1 and 4 and peaks 3 and 5 would ideally be mirror-images, vibrational coupling distorts the lineshapes of peaks 1 and 4. We thus fit only the $\Delta E \geq 0$ side (details in SI). Fit of the co-linear slice lineshape (Fig. 2c) gives a sideband (peaks 1 and 3) dephasing rate $\hbar\frac{\gamma_x + \gamma_y}{2} = 0.12$ meV (5.49 ps) and a zero-phonon line (peak 2) dephasing rate 0.124 meV (5.32 ps). Fit of peaks 4 and 5 in the cross-linear slice lineshape (Fig. 2d) gives a dephasing rate $\hbar\frac{\gamma_y + \gamma_z}{2} = 0.496$ meV (1.33 ps). The fitted triplet state energy splittings are likewise $\Omega_1 = 1.82$ meV and $\Omega_2 = 0.24$ meV. If the dipole moment of state $|\psi_y\rangle$ is indeed much larger than those of

$|\psi_x\rangle$ and $|\psi_z\rangle$, the zero-phonon line dephasing rate will approximately equal $\hbar\gamma_y$ which in turn determines the individual triplet state dephasing rates $\gamma_x = 0.116$ meV ($T_2^x = 5.68$ ps), $\gamma_y = 0.124$ meV ($T_2^y = 5.32$ ps), and $\gamma_z = 0.868$ meV ($T_2^z = 0.76$ ps).

ZERO-QUANTUM SPECTRA PROBE TERAHERTZ INTER-TRIPLET COHERENCES

Many of the quantum pathways that generate the sidebands in Figs. 2a and 2b involve inter-triplet coherences, which are quantum coherences between triplet states that are not necessarily dipole coupled [26]. Of both fundamental and practical importance is the inter-triplet coherence time, which defines the timescale during which the superposition states involved may be coherently manipulated. Inter-triplet coherences are those density matrix elements of the form $|\psi_i\rangle\langle\psi_j|$ where $i, j = \{x, y, z\}$ and $i \neq j$. To directly measure and characterize these coherences, we take zero-quantum spectra at varying temperature and delay τ . For co-linear excitation no inter-triplet coherences between $|\psi_x\rangle$ and $|\psi_y\rangle$ are observed (see SI). It is ambiguous whether their corresponding peaks are weak, or are simply obscured by the linewidth of a central $\omega_T = 0$ peak. For cross-linear excitation, we further isolate the inter-triplet coherence pathways by passing the measured FWM signal through a vertical polarizer. We plot a resultant cross-linear zero-quantum spectrum at 20 K in Fig. 3a. Sidebands are observed at mixing energies identical to the positions of peaks 4 and 5 in Fig. 2d, which we attribute to inter-triplet coherences between $|\psi_y\rangle$ and $|\psi_z\rangle$. An inter-triplet coherence between $|\psi_x\rangle$ and $|\psi_z\rangle$ is observed in neither the co-linear nor cross-linear zero-quantum spectra, which is consistent with a dominant transition dipole of state $|\psi_y\rangle$ as argued above.

In Fig. 3b, the evolutions of normalized slices (at $\hbar\omega_T = 1890$ meV) as a function of delay τ and temperature are shown. The FWM signal dephases rapidly with increasing τ and results in an equally rapid decrease of sideband visibility, in contrast to the opposite behavior of vibrational intraband coherences (see [16] and SI). No change in the amplitude ratio between sidebands 6 and 8 is observed as temperature increases, confirming that the state splitting observed indeed belongs to the bright-triplet excited state rather than from thermal filling of higher-lying ground states. We note that the triplet state coherences in one-quantum spectra broaden significantly with increasing temperature, and are not resolved at temperatures above 15 K. In contrast, no significant broadening is observed of the inter-triplet coherence linewidth up to 40 K (see Fig. 3b), indicating that inter-triplet coherences are robust against thermal dephasing [14].

A slice at $\tau = 0$ fs is plotted in Fig. 3c, from which we can extract the inter-triplet coherence time. How-

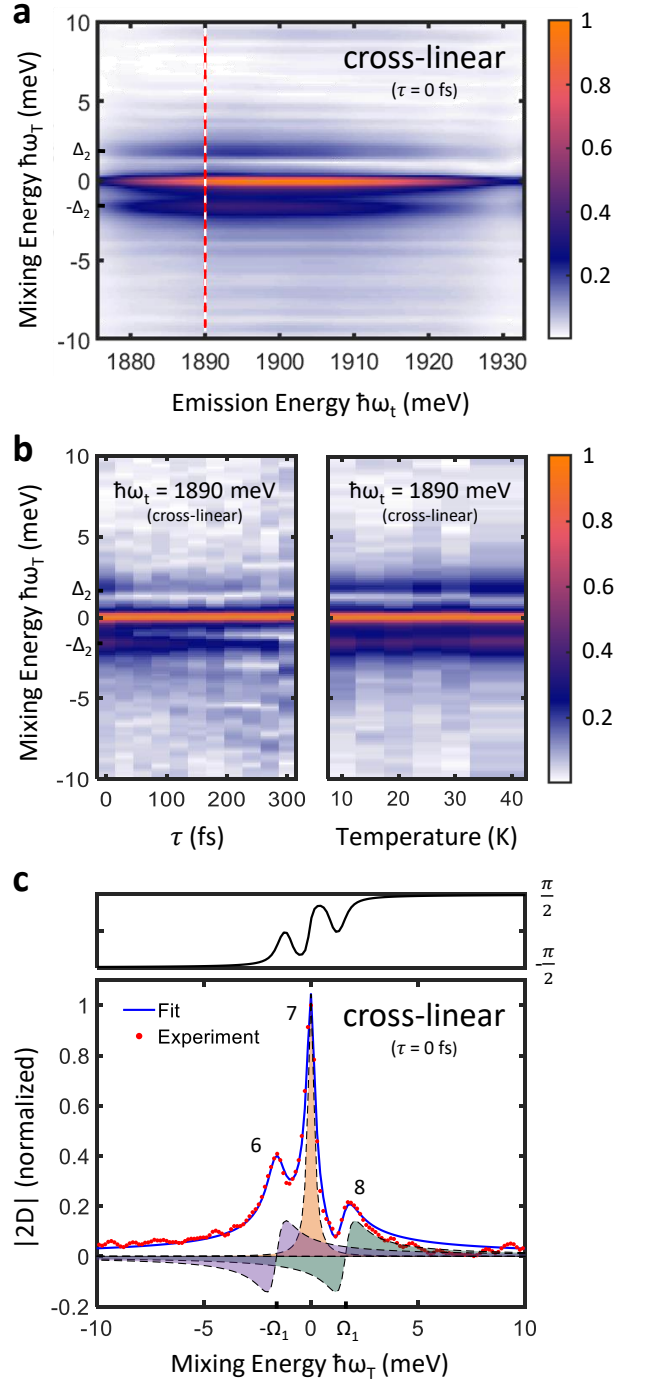


FIG. 3: **Inter-triplet coherences in zero-quantum spectra.** **a**, Magnitude zero-quantum spectrum taken at $\tau = 0$ fs and 20 K by passing the FWM signal through a vertical polarizer. Two sidebands due to inter-triplet coherences are observed. **b**, Evolution of normalized slices taken along the dashed red line in **a** at $\hbar\omega_t = 1890$ meV as a function of delay τ (at 20 K) and temperatures [10, 15, 20, 25, 30, 40] K (at $\tau = 0$ fs). **c**, Fit of cross-slice taken at $\tau = 0$ fs, in which the complex Lorentzians of peaks 6 and 8 are shifted by phases $-\frac{\pi}{2}$ relative to peak 7. The shaded curves represent the real quadratures of each Lorentzian used to fit lineshape, and the top plot is the phase of the fitted complex lineshape.

ever, the quantum pathways that generate peaks 6 and 8 involve identical dipole moments $\mu_y^2\mu_z^2$, from which we expect equal peak amplitudes contrary to the uneven peaks observed. This difference is due to interference between the three complex Lorentzian lineshapes underlying the overall amplitude lineshape, and the fit to experiment is performed by shifting the phase of each sideband Lorentzian lineshape by identical factors of $-\frac{\pi}{2}$ relative to the central $\omega_T = 0$ peak. From our fit, we extract an energy splitting $\Omega_1 = 1.61$ meV and an inter-triplet coherence time $T_2^{yz} = 1.36$ ps at 20 K.

DISCUSSION

It is quite unexpected that the optical dephasing rate γ_z is so much faster than those of the other two triplet states γ_x and γ_y . Although this disparity suggests a fundamentally different dephasing mechanism for coherences involving state $|\psi_z\rangle$, photoluminescence of similar orthorhombic perovskite NCs that exhibit triplet state structure reveals similar emission linewidths for all three states of the manifold [6, 7]. We resolve this discrepancy by proposing a unique exciton fine-structure comprised of a dark singlet state $|\psi_d\rangle$ that lies above the states $|\psi_x\rangle$ and $|\psi_y\rangle$, which form the band-edge, while remaining below the third triplet state $|\psi_z\rangle$ (shown in Fig. 1c). Rapid relaxation from $|\psi_z\rangle$ to $|\psi_d\rangle$ then significantly decreases the population lifetime T_1^z , and consequently T_2^z as well [24]. Such a fine-structure has been theoretically predicted [27] in certain ranges of NC size due to competition between the Rashba effect and electron-hole exchange interaction. Our hypothesis is further supported by previous photoluminescence studies of CsPbI₃ NCs of nearly identical size [10] which revealed polarized doublets corresponding to $|\psi_x\rangle$ and $|\psi_y\rangle$ but did not detect the third triplet state $|\psi_z\rangle$, whose emission would be quenched by non-radiative relaxation to $|\psi_d\rangle$ according to our model. In accordance with the predicted size-dependence of the relative dark state energy [27], we also observe an abrupt increase in T_2^y with increasing slice position (see SI) which results from a crossing in energy of $|\psi_y\rangle$ and $|\psi_d\rangle$.

To conclude, we have measured and characterized both optical frequency triplet coherences and terahertz frequency inter-triplet coherences. We have also presented evidence of an exciton bandedge whose emission is partially quenched by an intermediate dark state, which contributes important insight into the controversial nature of exciton ground states in different perovskite NC materials [6, 7]. As a material still in its infancy, perovskite NCs show promise for applications in opto-electronic devices. Particularly, the minimal thermal broadening of inter-triplet coherences observed here motivates study of applications above cryogenic temperatures. For example, in a triplet-state analogue of valleytronics in two-dimensional materials [19], superpositions of triplet states could be

initialized and read-out with linearly polarized light and coherently manipulated via terahertz radiation [28] as information carriers.

* These authors contributed equally.

† Electronic address: padilha@ifi.unicamp.br

‡ Electronic address: cundiff@umich.edu

- [1] L. Protesescu, S. Yakunin, M. I. Bodnarchuk, F. Krieg, R. Caputo, C. H. Hendon, R. X. Yang, A. Walsh, and M. V. Kovalenko, *Nano Letters* **15**, 3692 (2015), ISSN 1530-6984, URL <https://doi.org/10.1021/nl5048799>.
- [2] S.-T. Ha, R. Su, J. Xing, Q. Zhang, and Q. Xiong, *Chemical Science* **8**, 2522 (2017), ISSN 2041-6520, URL <http://dx.doi.org/10.1039/C6SC04474C>.
- [3] F. Liu, Y. Zhang, C. Ding, S. Kobayashi, T. Izuishi, N. Nakazawa, T. Toyoda, T. Ohta, S. Hayase, T. Minemoto, et al., *ACS Nano* **11**, 10373 (2017), ISSN 1936-0851, URL <https://doi.org/10.1021/acsnano.7b05442>.
- [4] L. Jaehoon, J. B. Guk, P. Myeongjin, K. J. Kyeong, P. J. M., P. Young-Shin, K. V. I., L. Changhee, L. D. C., and B. W. Ki, *Advanced Materials* **26**, 8034 (2014), ISSN 0935-9648, URL <https://doi.org/10.1002/adma.201403620>.
- [5] M. Nirmal, D. J. Norris, M. Kuno, M. G. Bawendi, A. L. Efros, and M. Rosen, *Physical Review Letters* **75**, 3728 (1995), URL <https://link.aps.org/doi/10.1103/PhysRevLett.75.3728>.
- [6] M. A. Becker, R. Vaxenburg, G. Nedelcu, P. C. Serce, A. Shabaev, M. J. Mehl, J. G. Michopoulos, S. G. Lambrakos, N. Bernstein, J. L. Lyons, et al., *Nature* **553**, 189 EP (2018), URL <http://dx.doi.org/10.1038/nature25147>.
- [7] P. Tamarat, M. I. Bodnarchuk, J.-B. Trebbia, R. Erni, M. V. Kovalenko, J. Even, and B. Lounis, *Nature Materials* **18**, 717 (2019), ISSN 1476-4660, URL <https://doi.org/10.1038/s41563-019-0364-x>.
- [8] G. Rainò, M. A. Becker, M. I. Bodnarchuk, R. F. Mahrt, M. V. Kovalenko, and T. Stöferle, *Nature* **563**, 671 (2018), ISSN 1476-4687, URL <https://doi.org/10.1038/s41586-018-0683-0>.
- [9] H. Utzat, W. Sun, A. E. K. Kaplan, F. Krieg, M. Ginterseder, B. Spokoyny, N. D. Klein, K. E. Shulenberg, C. F. Perkinson, M. V. Kovalenko, et al., *Science* **363**, 1068 (2019), URL <http://science.sciencemag.org/content/363/6431/1068.abstract>.
- [10] C. Yin, L. Chen, N. Song, Y. Lv, F. Hu, C. Sun, W. W. Yu, C. Zhang, X. Wang, Y. Zhang, et al., *Physical Review Letters* **119**, 026401 (2017), URL <https://link.aps.org/doi/10.1103/PhysRevLett.119.026401>.
- [11] L. Chen, B. Li, C. Zhang, X. Huang, X. Wang, and M. Xiao, *Nano Letters* **18**, 2074 (2018), ISSN 1530-6984, URL <https://doi.org/10.1021/acs.nanolett.8b00184>.
- [12] N. S. Makarov, S. Guo, O. Isaienko, W. Liu, I. Robel, and V. I. Klimov, *Nano Letters* **16**, 2349 (2016), ISSN 1530-6984, URL <https://doi.org/10.1021/acs.nanolett.5b05077>.
- [13] J. A. Castañeda, G. Nagamine, E. Yassitepe, L. G. Bonato, O. Voznyy, S. Hoogland, A. F. Nogueira, E. H. Sar-

- gent, C. H. B. Cruz, and L. A. Padilha, *ACS Nano* **10**, 8603 (2016), ISSN 1936-0851, URL <https://doi.org/10.1021/acsnano.6b03908>.
- [14] G. Moody, C. Kavir Dass, K. Hao, C.-H. Chen, L.-J. Li, A. Singh, K. Tran, G. Clark, X. Xu, G. Berghäuser, et al., *Nature Communications* **6**, 8315 EP (2015), article, URL <http://dx.doi.org/10.1038/ncomms9315>.
- [15] K. Hao, G. Moody, F. Wu, C. K. Dass, L. Xu, C.-H. Chen, L. Sun, M.-Y. Li, L.-J. Li, A. H. MacDonald, et al., *Nature Physics* **12**, 677 EP (2016), URL <http://dx.doi.org/10.1038/nphys3674>.
- [16] A. Liu, D. B. Almeida, W. K. Bae, L. A. Padilha, and S. T. Cundiff, *Physical Review Letters* **123**, 057403 (2019), URL <https://link.aps.org/doi/10.1103/PhysRevLett.123.057403>.
- [17] A. Liu, D. B. Almeida, W.-K. Bae, L. A. Padilha, and S. T. Cundiff, *The Journal of Physical Chemistry Letters* **10**, 6144 (2019), URL <https://doi.org/10.1021/acs.jpcllett.9b02474>.
- [18] S. T. Cundiff and S. Mukamel, *Physics Today* **66**, 44 (2013), ISSN 0031-9228, URL <https://doi.org/10.1063/PT.3.2047>.
- [19] J. R. Schaibley, H. Yu, G. Clark, P. Rivera, J. S. Ross, K. L. Seyler, W. Yao, and X. Xu, *Nature Reviews Materials* **1**, 16055 EP (2016), review Article, URL <http://dx.doi.org/10.1038/natrevmats.2016.55>.
- [20] A. Liu, L. G. Bonato, F. Sessa, D. B. Almeida, E. Isele, G. Nagamine, L. F. Zagonel, A. F. Nogueira, L. A. Padilha, and S. T. Cundiff, *The Journal of Chemical Physics* **151**, 191103 (2019), ISSN 0021-9606, URL <https://doi.org/10.1063/1.5124399>.
- [21] A. D. Bristow, D. Karauskaj, X. Dai, T. Zhang, C. Carlsson, K. R. Hagen, R. Jimenez, and S. T. Cundiff, *Review of Scientific Instruments* **80**, 073108 (2009), ISSN 0034-6748, URL <https://doi.org/10.1063/1.3184103>.
- [22] L. Yang, T. Zhang, A. D. Bristow, S. T. Cundiff, and S. Mukamel, *The Journal of Chemical Physics* **129**, 234711 (2008), ISSN 0021-9606, URL <https://doi.org/10.1063/1.3037217>.
- [23] M. E. Siemens, G. Moody, H. Li, A. D. Bristow, and S. T. Cundiff, *Optics Express* **18**, 17699 (2010), URL <http://www.opticsexpress.org/abstract.cfm?URI=oe-18-17-17699>.
- [24] S. Mukamel, *Principles of Nonlinear Optical Spectroscopy* (Oxford University Press, 1999), 1st ed.
- [25] M. A. Becker, L. Scarpelli, G. Nedelcu, G. Rainò, F. Masia, P. Borri, T. Stöferle, M. V. Kovalenko, W. Langbein, and R. F. Mahrt, *Nano Letters* **18**, 7546 (2018), ISSN 1530-6984, URL <https://doi.org/10.1021/acs.nanolett.8b03027>.
- [26] K. B. Ferrio and D. G. Steel, *Physical Review Letters* **80**, 786 (1998), URL <https://link.aps.org/doi/10.1103/PhysRevLett.80.786>.
- [27] P. C. Sercel, J. L. Lyons, D. Wickramaratne, R. Vaxenburg, N. Bernstein, and A. L. Efros, *Nano Letters* (2019), ISSN 1530-6984, URL <https://doi.org/10.1021/acs.nanolett.9b01467>.
- [28] F. Langer, C. P. Schmid, S. Schlauderer, M. Gmitra, J. Fabian, P. Nagler, C. Schüller, T. Korn, P. G. Hawkins, J. T. Steiner, et al., *Nature* **557**, 76 (2018), ISSN 1476-4687, URL <https://doi.org/10.1038/s41586-018-0013-6>.

Acknowledgements This work was supported by the Department of Energy grant number DE-SC0015782. D.B.A. and G.N. acknowledge support from the Brazilian National Council for Scientific and Technological Development (CNPq). L.A.P. acknowledges support from FAPESP (Project numbers 2013/16911-2 and 2016/50011-7). Research was also supported by LNNano/CNPEM/MCTIC, where the TEM measurements were performed.

Author Contributions A.L. and D.B.A. contributed equally to this work. L.A.P. and S.T.C. conceived the concept. L.G.B. synthesized the perovskite NC sample under supervision from A.F.N. G.N. and L.F.Z. acquired TEM images of the sample and characterized the NC size. A.L. and D.B.A. ran the experiments and acquired the data. A.L. analysed the results and wrote the manuscript. All authors discussed the results and commented on the manuscript at all stages.

Materials

The NCs studied are cube-shaped, with side lengths of 8.7 ± 2.6 nm measured from transmission electron microscopy measurements (shown in Fig. 1a). These sizes are comparable to the CsPbI₃ exciton Bohr diameter (12 nm) [1], and correspond to a room temperature 1S exciton absorption peak centered around 1900 meV (shown in Fig. 1b). The synthesis method is described in the SI.

Supplemental Information for:
Partially-Bright Triplet Excitons in Perovskite Nanocrystals

Contents

I. Sample Synthesis and Characterization	2
A. Preparation of Cs-Oleate Stock Solution	3
B. Synthesis of CsPbI ₃ perovskite nanocrystals with Cs:Pb:I = 1:4.34:8.68 Molar Ratio	3
C. Transmission Electron Microscopy (TEM)	4
II. Details of Experiment	4
III. Mapping Feynman Diagrams to Peaks in 2-D Spectra	5
A. Third-Order Response Function	5
B. Phase-Matching	6
C. Double-Sided Feynman Diagrams	6
D. Equation Form of Diagrams	7
IV. One-Quantum Lineshapes	8
Time-Domain Signal	8
New Transform Axes	9
Shift and Projection	10
Inhomogeneous Limit	10
V. Zero-Quantum Lineshapes	11
VI. One-Quantum Lineshape Fits	12
A. Co-linear Spectrum Fits	12
B. Cross-linear Spectrum Fits	13
VII. Co-Linear Zero-Quantum Spectra	15
References	15

I. SAMPLE SYNTHESIS AND CHARACTERIZATION

Synthesis of the nanocrystals used in this study follows the procedures detailed in [1, 2].

A. Preparation of Cs-Oleate Stock Solution

80 mg of Cs_2CO_3 (0.5 mM Cs^+) was added to a 50 mL 2-neck round-flask, followed by addition of 1 mL of oleic acid and 7 mL of 1-octadecene. The flask was connected to a Schlenk line and vigorously stirred under vacuum at 100°C for 1 hour. After obtaining a transparent solution ($[\text{Cs}^+] = 0.06$ mol/L), the system was maintained at 80°C under nitrogen flow to avoid the formation of a white precipitate.

B. Synthesis of CsPbI_3 perovskite nanocrystals with Cs:Pb:I = 1:4.34:8.68 Molar Ratio

100 mg of PbI_2 (≈ 0.217 mM) was added to a 50 mL 3-neck round-flask, followed by the addition of 4.5 mL of 1-octadecene. The flask was connected to a Schlenk line and vigorously stirred under vacuum at 100°C for 30 min. Afterwards 1 mL of oleic acid and 0.5 mL of oleylamine was added, while keeping the reaction flask under vigorous stirring in vacuum at 100°C until complete solubilization of the PbI_2 , upon obtaining a transparent yellow solution. Prior to injection of the Cs^+ precursor, the temperatures of the Pb^{2+} and I^- precursor solutions were raised to 140°C under vigorous stirring and nitrogen flow, followed by swift injection of 0.8 mL of Cs-oleate stock solution. Formation of an intense red colloidal suspension of CsPbI_3 nanocrystals was then observed. The suspension was immediately submerged in a cold water bath to cool down to room temperature for quenching nanocrystal growth.

The nanocrystals were cleaned by adding 15 mL of anhydrous methylacetate and centrifuged at 12000 rpm for 5 minutes. The supernatant was discarded and the precipitated nanocrystals were redispersed in anhydrous hexane.

C. Transmission Electron Microscopy (TEM)

Transmission electron micrographs were acquired on the CsPbI₃ sample:

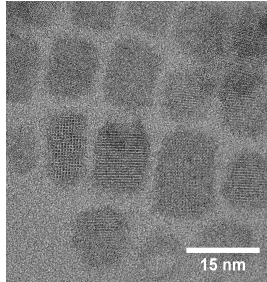


FIG. 1: Room-temperature TEM micrograph of CsPbI₃ nanocrystals.

100 nanocrystals were measured to obtain an average edge length 8.7 ± 2.6 nm.

II. DETAILS OF EXPERIMENT

We use a Multi-Dimensional Optical Nonlinear Spectrometer (MONSTR) [3], which focuses three laser pulses onto the sample. The excitation pulses are of 90 fs duration at a 250 kHz repetition rate, and the excitation intensity of 5 W/cm^2 generates a predominately third-order response as verified by a power-dependence measurement of the generated transient four-wave-mixing signal. The emitted signal is then heterodyne detected [4] with a co-propagating local-oscillator pulse as a function of time delays τ , T , and/or t with sub-wavelength stability.

The sample studied is an ensemble of CsPbI₃ perovskite nanocrystals dispersed in heptomethylnonane and suspended in a copper sample holder with sapphire windows. The sample optical density is measured to be 0.3 at the room-temperature 1S exciton absorption peak.

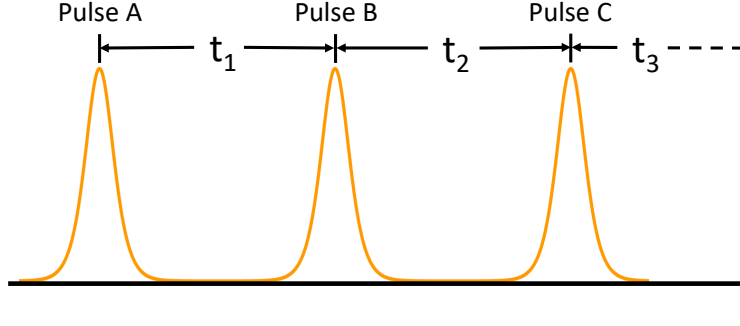
III. MAPPING FEYNMAN DIAGRAMS TO PEAKS IN 2-D SPECTRA

A. Third-Order Response Function

The interpretation of 2-D spectra is performed through a perturbative expansion of the material polarization in response to a weak field. The third-order response may be written as:

$$P^{(3)}(t) \propto \int_0^\infty \int_0^\infty \int_0^\infty E(t-t_3)E(t-t_3-t_2)E(t-t_3-t_2-t_1)R(t_3, t_2, t_1)dt_1dt_2dt_3 \quad (1)$$

where the times t_1 , t_2 , and t_3 are defined:



There is thus a direct correspondence between each field term in the third-order polarization and a single pulse in a three-pulse experiment. Note that what we denote t_1 , t_2 , and t_3 here are equivalent to the delays τ , T , and t respectively (as denoted in the main paper).

The response function $R(t_3, t_2, t_1)$ is defined by:

$$R^{(3)}(t_3, t_2, t_1) = -i\text{Tr} \{ \hat{\mu}(t_3 + t_2 + t_1), [\hat{\mu}(t_2 + t_1), [\hat{\mu}(t_1), [\hat{\mu}(0), \rho(t_0)]]] \} \quad (2)$$

where $\rho(t_0)$ is the initial density matrix of the system (which we take to be the ground state density matrix $|g\rangle\langle g|$), $\text{Tr}\{\dots\}$ denotes the trace operation and $\hat{\mu}(t)$ is the dipole operator in the interaction picture. We see that the response function is composed of three nested commutators, and thus contains 8 terms.

B. Phase-Matching

We see in equation (1) that there are three fields that each may be written in complex form:

$$E(t) \propto \mathcal{E}(t) (e^{+i\omega t - i\mathbf{k}\cdot\mathbf{r} - i\phi} + e^{-i\omega t + i\mathbf{k}\cdot\mathbf{r} + i\phi}) \quad (3)$$

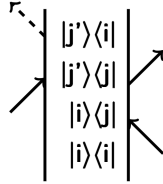
where ω and \mathbf{k} are the angular frequency and wavevector that characterize the electromagnetic wave, and $\mathcal{E}(t)$ is the pulse envelope.

In equation (2), the dipole operators are written in the interaction picture. This means they involve both interactions via the dipole operator $\hat{\mu}$ and density matrix evolution at the transition frequency ω_{ij} , where $|i\rangle$ and $|j\rangle$ are two states separated by the optical frequency we excite at. After taking into account both the optical field terms in equation (3) and the density matrix evolution terms, various terms will become negligible in the rotating wave approximation (RWA).

That is, for certain combinations $\pm\omega_A \pm \omega_B \pm \omega_C$ (and equivalently $\pm\mathbf{k}_A \pm \mathbf{k}_B \pm \mathbf{k}_C$), only certain terms of the nested commutator in equation (2) will be non-negligible. In our experiment, we isolate the polarization that radiates in the direction $\mathbf{k} = -\mathbf{k}_A + \mathbf{k}_B + \mathbf{k}_C$, and therefore isolate specific terms via *wave-vector selection*. The tedious process of calculating the explicit terms that survive the RWA may be considerably simplified by use of double-sided Feynman diagrams.

C. Double-Sided Feynman Diagrams

As mentioned above, in our experiment we isolate the radiated signal in the $\mathbf{k} = -\mathbf{k}_A + \mathbf{k}_B + \mathbf{k}_C$ direction. Because of the minus sign in front of \mathbf{k}_A , we say that pulse *A* is *conjugated*, while pulses B and C are *non-conjugated*. With these terms defined, we may construct the Feynman diagrams used to interpret the collected signal. An example diagram is shown:



where $|i\rangle$ is lower in energy with respect to $|j\rangle$ and $|j'\rangle$. The states $|i\rangle$ and $|j\rangle/|j'\rangle$ are separated by $\hbar\omega_{ij}/\hbar\omega_{ij'}$, where $\omega_{ij}/\omega_{ij'}$ are optical frequencies we excite at.

The diagram may be constructed as follows:

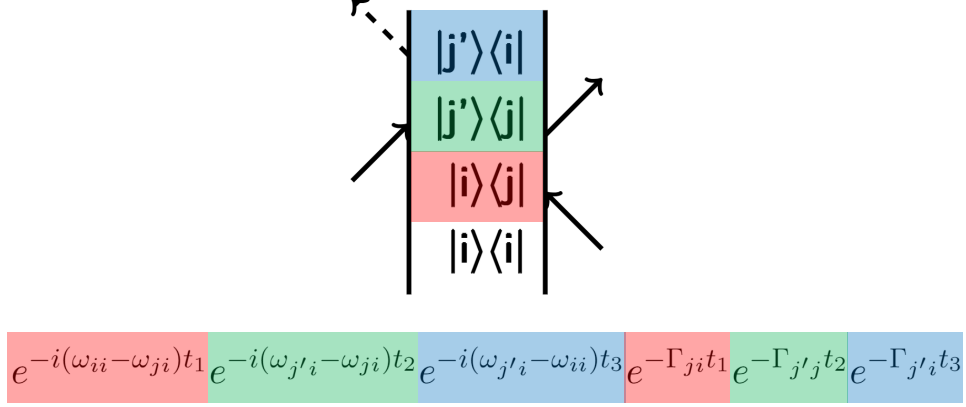
1. Time increases from the bottom of the diagram going up.
2. The density matrix element at the bottom $|i\rangle\langle i|$ is the initial density matrix of the system and must be a population state.
3. Pulse interactions are represented by arrows; arrows pointing (out)inwards cause (de)excitation of either the Ket or Bra, depending on the side on which the arrow is placed.
4. Ordering of the arrows going from the bottom upwards follows the time-ordering of the pulses in experiment.
5. Conjugated pulses are represented by left-pointing arrows, and non-conjugated pulses are represented by right-pointing arrows.
6. For a n -order process, there are n arrows and n density matrix elements after the initial density matrix $|i\rangle\langle i|$.

All diagrams that contribute to the measured signal may be found by taking all combinations of density matrix elements and arrows on either side that satisfy the above rules.

D. Equation Form of Diagrams

We now demonstrate how one may write down the relevant third-order polarization terms directly from the double-sided Feynman diagrams. We show the example diagram from before and its corresponding equation:

Here, we've highlighted each density matrix element and its corresponding terms in equation form. We see that the density matrix element induced by each pulse will oscillate at the difference frequency of the two states composing the Bra and Ket for a time t_i until the next excitation pulse or detection. For simplicity, we've included the Markovian dephasing terms Γ_{ij} , which correspond to either coherence dephasing (if $i \neq j$) or population relaxation



(if $i = j$). If the coherences evolve outside of the Markovian dephasing regime, we replace these terms by those of the form $e^{-g(t)}$, where $g(t)$ is the lineshape function characterizing the system-bath interaction.

IV. ONE-QUANTUM LINESHAPES

We show straightforward extensions of the procedure outlined by Siemens et al. [5] to fit lineshapes of sidebands in one-quantum and zero-quantum spectra.

Time-Domain Signal

We consider the case of a rephasing signal resulting from excitation and emission frequencies ω_1 and ω_2 respectively (ignoring dynamics during T), and assume perfectly correlated inhomogeneous broadening between the two transitions with dephasing rates γ_1 and γ_2 :

$$\begin{aligned}
 s(t, \tau) &= \Theta(t)\Theta(\tau)e^{-\gamma_1\tau}e^{-\gamma_2t} \int e^{-i[(\omega_1+\Delta\omega)\tau-(\omega_2+\Delta\omega)t]} e^{-\frac{\Delta\omega^2}{2\sigma^2}} d\Delta\omega \\
 &= \Theta(t)\Theta(\tau)e^{-\gamma_1\tau}e^{-\gamma_2t} e^{-i\omega_1\tau} e^{+i\omega_2t} \mathcal{F} \left\{ e^{-\frac{\Delta\omega^2}{2\sigma^2}} \right\} \Big|_{t-\tau} \\
 &\propto \Theta(t)\Theta(\tau)e^{-\gamma_1\tau}e^{-\gamma_2t} e^{-i\omega_1\tau} e^{+i\omega_2t} e^{-\frac{\sigma^2}{2}(t-\tau)^2}
 \end{aligned} \tag{4}$$

Defining the new time variables:

$$t' = \frac{1}{2}(t + \tau) \quad \tau' = \frac{1}{2}(t - \tau) \tag{5}$$

We recast the time-domain signal:

$$s(t', \tau') = \Theta(t' + \tau')\Theta(t' - \tau')e^{-\gamma_1(t' - \tau')}e^{-\gamma_2(t' + \tau')}e^{-i\omega_1(t' - \tau')}e^{+i\omega_2(t' + \tau')}e^{-2\sigma^2\tau'^2} \quad (6)$$

New Transform Axes

It is important to determine the specific axes that the new time-variables result in after Fourier transform. Writing out the original transform:

$$f(t, \tau) = \iint e^{-i(\omega_t t + \omega_\tau \tau)} f(\omega_t, \omega_\tau) d\omega_\tau d\omega_t \quad (7)$$

In terms of the new time variables:

$$\begin{aligned} f(t', \tau') &= \iint e^{-i[\omega_t(t' + \tau') + \omega_\tau(t' - \tau')]} f(\omega_t, \omega_\tau) d\omega_\tau d\omega_t \\ &= \iint e^{-i[(\omega_t + \omega_\tau)t' + (\omega_t - \omega_\tau)\tau']} f(\omega_t, \omega_\tau) d\omega_\tau d\omega_t \end{aligned}$$

We see that the natural conjugate variables for t' and τ' are:

$$\omega_{t'} = \omega_t + \omega_\tau \quad \omega_{\tau'} = \omega_t - \omega_\tau \quad (8)$$

or equivalently:

$$\omega_t = \omega_{t'} + \omega_{\tau'} \quad \omega_\tau = \omega_{t'} - \omega_{\tau'} \quad (9)$$

NOTE: In the rephasing pulse sequence, ω_τ is negative.

Using the Jacobian of our variable transformation:

$$J = \begin{vmatrix} \frac{d\omega_t}{d\omega_{t'}} & \frac{d\omega_t}{d\omega_{\tau'}} \\ \frac{d\omega_\tau}{d\omega_{t'}} & \frac{d\omega_\tau}{d\omega_{\tau'}} \end{vmatrix} = -1 - 1 = -2 \quad (10)$$

We change the variables of integration:

$$f(t', \tau') = 2 \iint e^{-i(\omega_{t'} t' + \omega_{\tau'} \tau')} f(\omega_{t'}, \omega_{\tau'}) d\omega_{\tau'} d\omega_{t'} \quad (11)$$

Shift and Projection

We now shift the signal to the origin in our τ' and t' coordinates via multiplication by $e^{+i\omega_1(t'-\tau')\tau'} e^{-i\omega_2(t'+\tau')\tau'}$:

$$s_{origin}(t', \tau') = \Theta(t' + \tau')\Theta(t' - \tau')e^{-\gamma_1(t'-\tau')}e^{-\gamma_2(t'+\tau')}e^{-2\sigma^2\tau'^2} \quad (12)$$

The projections along t' and τ' are then:

$$s_{proj,t'} = \int_{-\infty}^{\infty} s_{origin}(t', \tau')d\tau' = e^{-(\gamma_1+\gamma_2)t'} \int_{-t'}^{t'} e^{(\gamma_1-\gamma_2)\tau'} e^{-2\sigma^2\tau'^2} d\tau' \quad (13)$$

$$s_{proj,\tau'} = \int_{-\infty}^{\infty} s_{origin}(t', \tau')dt' = e^{(\gamma_1-\gamma_2)\tau'} e^{-2\sigma^2\tau'^2} \int_{|\tau'|}^{\infty} e^{-(\gamma_1+\gamma_2)t'} dt' \quad (14)$$

where the Heaviside functions are accounted for by change of integration limits.

Inhomogeneous Limit

In the inhomogeneous limit ($\sigma \gg \gamma_1, \gamma_2$) the signal decays along τ' much faster than along t' . In the integral along τ' we can approximate the gaussian portion of the kernel as a delta function. In the integral along t' , we can approximate the lower limit as 0. These two limits give:

$$s_{proj,t'} = e^{-(\gamma_1+\gamma_2)t'} \int_{-t'}^{t'} e^{(\gamma_1-\gamma_2)\tau'} \delta(\tau')d\tau' = e^{-(\gamma_1+\gamma_2)t'} \Theta(t') \quad (15)$$

$$s_{proj,\tau'} = e^{(\gamma_1-\gamma_2)\tau'} e^{-2\sigma^2\tau'^2} \int_0^{\infty} e^{-(\gamma_1-\gamma_2)t'} dt' = e^{(\gamma_1-\gamma_2)\tau'} e^{-2\sigma^2\tau'^2} \quad (16)$$

which then give the frequency domain lineshapes in the inhomogeneous limit:

$$S_{slice}(\omega_{t'}) \propto \frac{1}{(\gamma_1 + \gamma_2) + i\omega_{t'}} \quad (\text{Cross-Diagonal}) \quad (17)$$

$$S_{slice}(\omega_{\tau'}) \propto e^{-\frac{\omega_{\tau'}^2}{8\sigma^2}} \quad (\text{Diagonal}) \quad (18)$$

where we've assumed $\gamma_1 - \gamma_2 \ll \sigma$.

V. ZERO-QUANTUM LINESHAPES

The lineshapes of a zero-quantum spectrum can be derived by the same method, with inclusion of an intermediate zero-quantum coherence with a dephasing rate of γ_T :

$$\begin{aligned}
s(t, T, \tau) &= \Theta(t)\Theta(T)\Theta(\tau)e^{-\gamma_1\tau}e^{-\gamma_2t}e^{-\gamma_T T} \int e^{-i[(\omega_1+\Delta\omega)\tau-(\omega_2+\Delta\omega)t]} e^{i(\omega_2-\omega_1)T} e^{-\frac{\Delta\omega^2}{2\sigma^2}} d\Delta\omega \\
&= \Theta(t)\Theta(T)\Theta(\tau)e^{-\gamma_1\tau}e^{-\gamma_2t}e^{-\gamma_T T} e^{+i(\omega_2-\omega_1)T} e^{-i\omega_1\tau} e^{+i\omega_2t} \int e^{+i\Delta\omega(t-\tau)} e^{-\frac{\Delta\omega^2}{2\sigma^2}} d\Delta\omega \\
&= \Theta(t)\Theta(T)\Theta(\tau)e^{-\gamma_1\tau}e^{-\gamma_2t}e^{-\gamma_T T} e^{+i(\omega_2-\omega_1)T} e^{-i\omega_1\tau} e^{+i\omega_2t} \mathcal{F} \left\{ e^{-\frac{\Delta\omega^2}{2\sigma^2}} \right\} \Big|_{t-\tau} \\
&= \Theta(t)\Theta(T)\Theta(\tau)e^{-\gamma_1\tau}e^{-\gamma_2t}e^{-\gamma_T T} e^{+i(\omega_2-\omega_1)T} e^{-i\omega_1\tau} e^{+i\omega_2t} \left[e^{-\frac{\sigma^2}{2}t'^2} \right]_{t'=t-\tau} \\
&= \Theta(t)\Theta(T)\Theta(\tau)e^{-\gamma_1\tau}e^{-\gamma_2t}e^{-\gamma_T T} e^{+i(\omega_2-\omega_1)T} e^{-i\omega_1\tau} e^{+i\omega_2t} e^{-\frac{\sigma^2}{2}(t-\tau)^2} \tag{19}
\end{aligned}$$

Shift frequency domain peak to origin:

$$\begin{aligned}
s_{origin}(t, T, \tau) &= s(t, T, \tau) e^{-i(\omega_2-\omega_1)T} e^{-i\omega_2t} \\
&= \Theta(t)\Theta(T)\Theta(\tau) e^{-\gamma_1\tau} e^{-\gamma_2t} e^{-\gamma_T T} e^{-i\omega_1\tau} e^{-\frac{\sigma^2}{2}(t-\tau)^2} \tag{20}
\end{aligned}$$

Project onto T axis:

$$\begin{aligned}
s_{proj}(T) &= \int_{-\infty}^{\infty} s_{origin}(t, T, \tau) dt \\
&= \Theta(t)\Theta(T)\Theta(\tau) e^{-\gamma_1\tau} e^{-\gamma_T T} e^{-i\omega_1\tau} \int_0^{\infty} e^{-\gamma_2t} e^{-\frac{\sigma^2}{2}(t-\tau)^2} dt \\
&= \Theta(t)\Theta(T)\Theta(\tau) e^{-(\gamma_1+\gamma_2)\tau} e^{-\gamma_T T} e^{-i\omega_1\tau} \int_{-\tau}^{\infty} e^{-\gamma_2t'} e^{-\frac{\sigma^2}{2}t'^2} dt' \tag{21}
\end{aligned}$$

In the inhomogeneous limit:

$$s_{proj}(T) = \Theta(t)\Theta(T)\Theta(\tau) e^{-(\gamma_1+\gamma_2)\tau} e^{-\gamma_T T} e^{-i\omega_1\tau} \tag{22}$$

which gives the lineshape:

$$\begin{aligned}
S_{slice}(\omega_T) &= \Theta(t)\Theta(\tau) e^{-(\gamma_1+\gamma_2)\tau} e^{-i\omega_1\tau} \mathcal{F} \left\{ e^{-\gamma_T T} \Theta(T) \right\} \\
&\propto \Theta(t)\Theta(\tau) e^{-(\gamma_1+\gamma_2)\tau} e^{-i\omega_1\tau} \frac{1}{\gamma_T - i\omega_T} \tag{23}
\end{aligned}$$

VI. ONE-QUANTUM LINESHAPE FITS

The lineshapes observed in the obtained one-quantum spectra, especially on the $\Delta E < 0$ side of each spectra, exhibit lineshapes distorted by vibrational coupling that deviate from ideal summations of Lorentzians. We thus fit the co-linear and cross-linear lineshapes with symmetric complex Lorentzian peaks, but only on the $\Delta E \geq 0$ side.

A. Co-linear Spectrum Fits

To investigate the dependence of parameters on nanocrystal size, we fit cross-diagonal slices centered at various slice positions $|\hbar\omega_\tau| = |\hbar\omega_t|$:

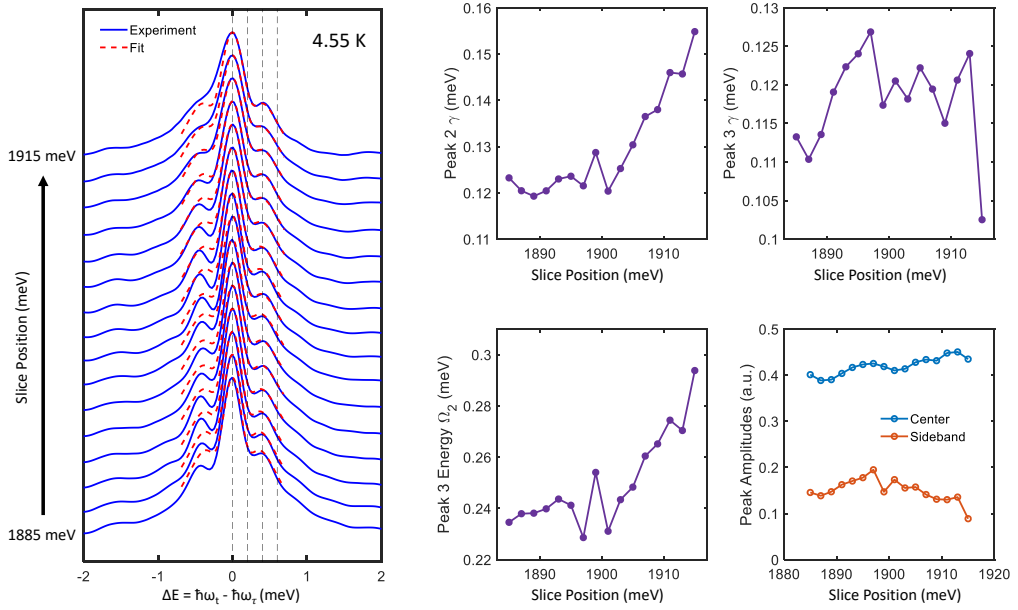


FIG. 2: Left: The slices from a co-linear one-quantum spectrum at 4.55 K are plotted as blue curves, with their corresponding fitted lineshapes overlaid as dashed red lines. Right: Fitted parameters are plotted as a function of slice position.

The slices are fitted in the range $0 \leq \Delta E \leq 0.7$ meV to three complex Lorentzians, where the sidebands are shifted in phase by $\frac{\pi}{2}$ to achieve the correct lineshapes.

B. Cross-linear Spectrum Fits

Just as with the co-linear spectrum, we fit cross-diagonal slices centered at various slice positions $|\hbar\omega_\tau| = |\hbar\omega_t|$:

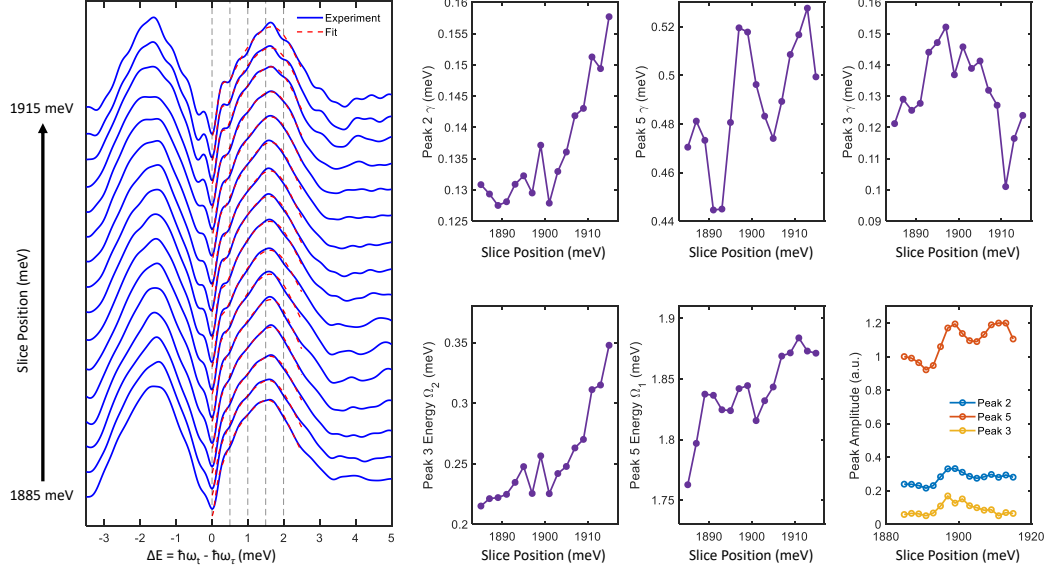


FIG. 3: Left: The slices from cross-linear one-quantum spectra are plotted as blue curves, with their corresponding fitted lineshapes overlaid as dashed red lines. Right: Fitted parameters are plotted as a function of slice position.

The slices are fitted in the range $0 \leq \Delta E \leq 2.5$ meV to five complex Lorentzians, where all four sidebands are shifted in phase by $\pi/2$ to achieve the correct lineshapes. To explore the possibility of a weak, third sideband at energy $\Delta E = \Omega_1 + \Omega_2$, corresponding to absorption and emission involving the states $|\psi_x\rangle$ and $|\psi_z\rangle$, we attempted to fit the above lineshapes with an additional two Lorentzian peaks. However, no reasonable fits were found possible.

From the fitted peak linewidths, we can extract the dephasing rates of the triplet state manifold γ_x , γ_y , and γ_z as described in the main text:

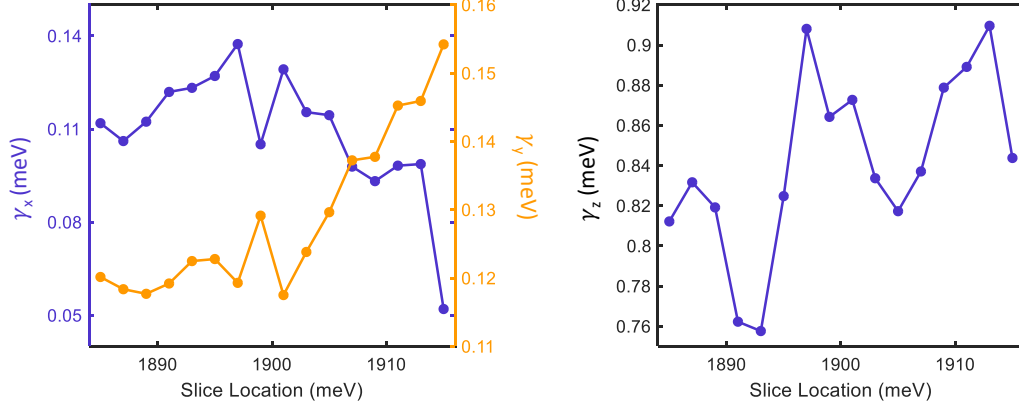


FIG. 4: Extracted dephasing rates of each triplet state transition.

While γ_x does not exhibit a clear monotonic increase or decrease with changing size, γ_y sharply increases at a slice position of around 1900 meV. This indicates that, within the size-distribution probed by our laser bandwidth, $|\psi_y\rangle$ becomes degenerate with $|\psi_d\rangle$ at an energy gap of around 1900 meV and becomes increasingly higher in energy at larger slice positions. A more statistically comprehensive study is needed to draw firm quantitative conclusions.

VII. CO-LINEAR ZERO-QUANTUM SPECTRA

Zero-quantum spectra were acquired with a co-linear (HHHH) excitation scheme:

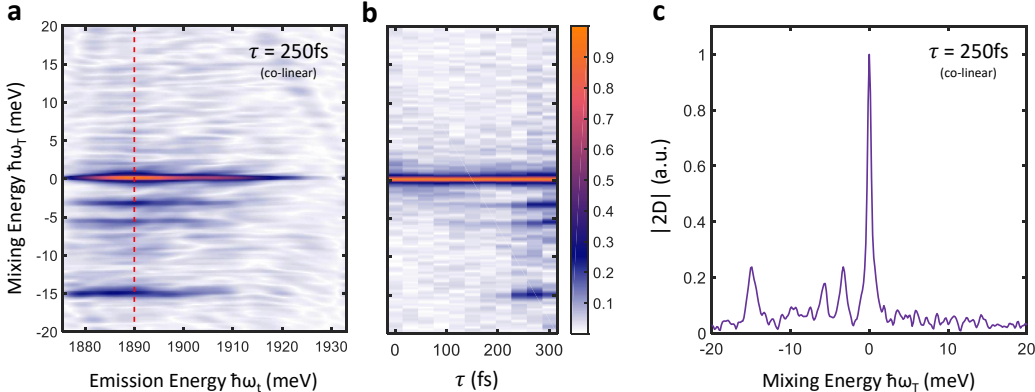


FIG. 5: (a) Zero-quantum spectra taken with co-linear excitation at $\tau = 250$ fs. (b) Evolution of normalized slices taken at $\hbar\omega_t = 1890$ meV (indicated by the dashed red line in figure a). (c) Normalized cross-slice taken at $\tau = 250$ fs and $\hbar\omega_t = 1890$ meV (indicated by the dashed red line in figure a).

No inter-triplet coherences were observed, which are expected to be symmetric in positive and negative mixing energy due to their electronic origin. However, multiple negative mixing energy sidebands appear with increasing delay τ , which we attribute to electronic-vibrational coupling and discuss in a separate paper.

[1] L. Protesescu, S. Yakunin, M. I. Bodnarchuk, F. Krieg, R. Caputo, C. H. Hendon, R. X. Yang, A. Walsh, and M. V. Kovalenko, *Nano Letters* **15**, 3692 (2015), ISSN 1530-6984, URL <https://doi.org/10.1021/nl15048779>.

[2] L. Protesescu, S. Yakunin, S. Kumar, J. Bär, F. Bertolotti, N. Masciocchi, A. Guagliardi, M. Grotevent, I. Shorubalko, M. I. Bodnarchuk, et al., *ACS Nano* **11**, 3119 (2017), ISSN 1936-0851, URL <https://doi.org/10.1021/acsnano.7b00116>.

[3] A. D. Bristow, D. Karaiskaj, X. Dai, T. Zhang, C. Carlsson, K. R. Hagen, R. Jimenez, and S. T. Cundiff, *Review of Scientific Instruments* **80**, 073108 (2009), ISSN 0034-6748, URL <https://doi.org/10.1063/1.313108>.

[//doi.org/10.1063/1.3184103](http://doi.org/10.1063/1.3184103).

- [4] L. Lepetit, G. Chériaux, and M. Joffre, *Journal of the Optical Society of America B* **12**, 2467 (1995), URL <http://josab.osa.org/abstract.cfm?URI=josab-12-12-2467>.
- [5] M. E. Siemens, G. Moody, H. Li, A. D. Bristow, and S. T. Cundiff, *Optics Express* **18**, 17699 (2010), URL <http://www.opticsexpress.org/abstract.cfm?URI=oe-18-17-17699>.